

Angular Scattering Pattern of Femtosecond Laser-Induced Refractive Index Modifications in Optical Fibers

Aaron Reupert, Maximilian Heck, Stefan Nolte, and Lothar Wondraczek*

Focused femtosecond laser irradiation is used to induce light scattering modifications in the core of an optical fiber. This turns the fiber into a diffuse, line-shaped light source. The scattering is investigated by imaging almost the full solid angle far-field pattern for the first time. Additionally, an electromagnetic scattering model is developed to explain the observations. The findings herein change how the relationship between light scattering and the refractive index fluctuations is perceived by showing that the far-field scattering pattern is the power spectral density of the polarization current inside the scattering center. Further, the authors contribute to a better estimation of the scattering process by showing that the total scattering power scales quadratically with the laser-induced refractive index change and its volume.

1. Introduction

Light scattering normally constitutes undesired loss in optical fibers. However, if harnessed appropriately, it can be used to turn an optical fiber into a flexible line-shaped light source. Such side-emitting fiber underlies several real and potential applications, for example, in endoscopy where physical access is difficult, and a thin, non-conductive, and chemically stable light source is necessary.^[1–3]

Early research of light scattering in optical fibers focused on the loss aspect. The field was pioneered by Marcuse, describing intrinsic fiber loss in the framework of electromagnetic theory which he attributed to fluctuations in the core cladding

interface, or in the glass matrix itself.^[4–6] Rawson measured the angular scattering spectrum of a pristine optical fiber for the first time and linked it to the presence of small needle-like structures for which he also gave a theoretical description.^[7]

More recent experimental research has turned toward the scattering loss of laser-induced microstructures like fiber Bragg gratings (FBGs) and long-period fiber gratings (LPFGs). Fonjallaz et al. and Janos et al. found an azimuthal scattering dependency, where the weakest intensity was measured in the direction of the laser irradiation which created the modifications.^[8,9] Vesselov et al. on the other hand

used light scattering on long-period fiber gratings to generate customizable side emission.^[10] We showed previously how deliberately placed femtosecond laser-induced refractive index distortions can be used to create light diffusing fiber segments with a customizable emission profile.^[11]

Meanwhile, the idea of deterministic scattering on tilted fiber gratings gave rise to further theoretical development of coupling guided to radiation modes. Here, two lines of analysis were followed: the mode coupling theory and the volume current method. While the first is deemed to be more exact, the second offers a more intuitive understanding of the scattering effect. Li et al. showed that both approaches are in good agreement, except for very low scattering angles.^[12]


Vesselov,^[10] as well as our prior study^[11] relied on a phenomenological model of scattering loss which cannot describe the relation between the refractive index modification and the scattering power or the angular emission profile. These shortcomings will be addressed in the present paper, where we develop a new approach to the electromagnetic description of the scattering process based on the volume current method. From this, we are able to explain and predict the angular scattering pattern of refractive index modifications just by using Fourier transforms and convolutions. These mathematical tools are simple to implement with current computer technology. As it turns out, this method can be applied equally well to scattering of all kinds of structures in optical fibers, be it desired or undesired.

For experimental comparison, we study chains of refractive index modifications in the core of a few-mode optical fiber which we created with focused femtosecond laser pulses. Such irradiation has the advantage over a continuous wave laser in that it can modify the refractive index in any transparent material and can induce strong refractive index fluctuations which scatter light.^[13] The investigation of the refractive index modification and far-field scattering pattern was done with the help of

A. Reupert, Prof. L. Wondraczek
Otto Schott Institute of Materials Research
Friedrich-Schiller-Universität Jena
Fraunhoferstr. 6, Jena 07743, Germany
E-mail: lothar.wondraczek@uni-jena.de

Dr. M. Heck, Prof. S. Nolte
Institute of Applied Physics
Abbe Center of Photonics
Friedrich-Schiller-Universität Jena
Albert-Einstein-Str. 15, Jena 07745, Germany

Prof. S. Nolte
Fraunhofer Institute for Applied Optics and Precision Engineering
Albert-Einstein-Str. 7, Jena 07745, Germany

 The ORCID identification number(s) for the author(s) of this article can be found under <https://doi.org/10.1002/adom.202000633>.

© 2020 The Authors. Published by WILEY-VCH Verlag GmbH & Co. KGaA, Weinheim. This is an open access article under the terms of the Creative Commons Attribution-NonCommercial License, which permits use, distribution and reproduction in any medium, provided the original work is properly cited and is not used for commercial purposes.

DOI: 10.1002/adom.202000633

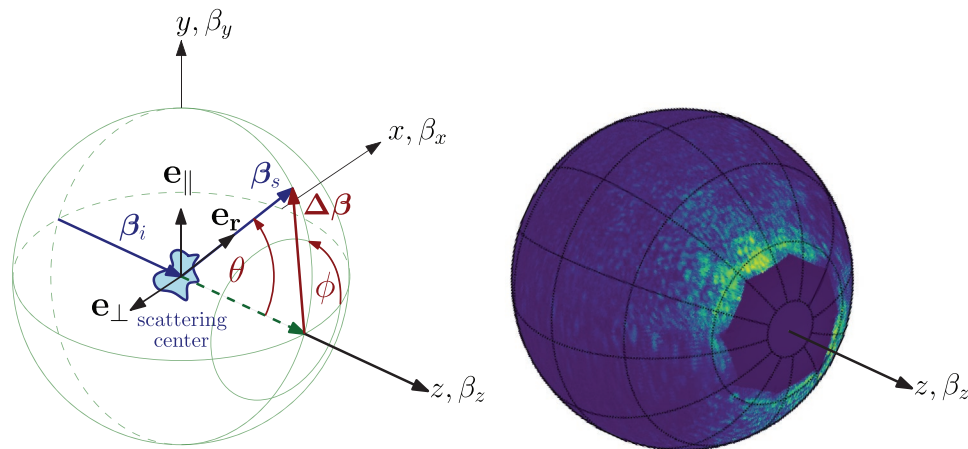


Figure 1. Schematics (left) and experimental data (right) of the far-field scattering pattern of a refractive index modification located in the middle of the sphere. β_i is the wave vector of the incoming light with the polarization directions \mathbf{e}_\perp and \mathbf{e}_\parallel . β_s is the wave vector of the scattered light, which spans the polar angle θ with respect to the incoming wave. $\Delta\beta$ is the scattering vector. ϕ is the azimuthal angle of the scattered light.

several microscopy methods, that is, shearing, phase-contrast, and Fourier microscopy. A combination with modern digital image processing techniques allowed us to visualize almost the whole solid angle of the far-field scattering pattern of a refractive index modification in an optical fiber for the first time.

The paper is organized as follows: Section 2 presents the derivation of the far-field scattering pattern of a localized refractive index perturbation in a multimode optical fiber. Section 3 describes the experimental conditions for the creation of the refractive index modification as well as the microscopy techniques for measuring the far-field scattering pattern. Section 4 examines the results of the laser processing and scattering measurements, which we discuss in Section 5 and compare the results with the theory from Section 2.

2. Theory: Light Scattering on Stochastic Distortions

When guided light interacts with a (laser-induced) refractive index modification Δn in an optical fiber it is scattered in all directions with varying power. This results in an angular spectrum of the scattered radiation which can be pictured on the unit sphere (Figure 1).

In this section, we show that this spectrum is closely related to the power spectrum and the shape of the refractive index distortion by applying a perturbation technique called volume current method.^[14,15] Here, the interaction of the distortion Δn with the guided electromagnetic field \mathbf{E}_0 induces a polarization current density \mathbf{j} inside the volume (boldface letters denote vectors). This current radiates light \mathbf{E}_s which effectively results in power being removed from the incident field. This scattering process is described by the inhomogeneous Helmholtz equation:

$$\nabla \times (\nabla \times \mathbf{E}_s) - n_0^2 k^2 \mathbf{E}_s = 2n_0 \Delta n k^2 \mathbf{E}_0 = -i\omega\mu_0 \mathbf{j} \quad (1)$$

where the refractive index difference between fiber core and cladding has been neglected for simplicity. The interaction of the guided electric field with the perturbation causes a

scattered electromagnetic field which is driven by the current density $\mathbf{j} = 2i\omega n_0 \Delta n \epsilon_0 \mathbf{E}_0$. Outside the perturbation Δn is zero and the differential equation is homogeneous, so the solution is the standard eigenmode expansion of the incoming incident field

$$\mathbf{E}_0(\mathbf{r}) = \sum_{\mu}^{\max} c_{\mu}(z) \mathbf{E}_{\mu}(x, y) e^{i\beta_{\mu} z} \quad (2)$$

which we assume to be transversal and unpolarized or circularly polarized. For the scattered field we use a standard procedure to solve the inhomogeneous Helmholtz equation with the aid of a vector potential \mathbf{A} and the Lorentz gauge.^[15] The solution outside of the fiber core in terms of the scattered electric and magnetic field strength is

$$\mathbf{E}_s = i\omega \mathbf{e}_r \times (\mathbf{e}_r \times \mathbf{A}_f), \quad \mathbf{H}_s = -\frac{in_0 k}{\mu_0} (\mathbf{e}_r \times \mathbf{A}_f) \quad (3)$$

Here \mathbf{A}_f is the far-field vector potential, made up by the superposition of outgoing spherical wavelets caused by the currents $\mathbf{j}(\mathbf{r}')$ enclosed in the volume V_0 of our scattering center:

$$\mathbf{A}_f = \frac{\mu_0}{4\pi} \frac{e^{in_0 k r}}{r} \int_{V_0} e^{-in_0 k \mathbf{e}_r \cdot \mathbf{r}'} \mathbf{j}(\mathbf{r}') dV' \quad (4)$$

Now, we calculate the pointing vector $\mathbf{S} = 1/2(\mathbf{E}_s \times \mathbf{H}_s^*)$ to obtain the direction and intensity of the far-field scattered radiation (* denotes the complex conjugate). For that, we perform the integration from Equation (4) two times, which we denote with the two integration variables \mathbf{r}_1 and \mathbf{r}_2 and their corresponding differential volume elements dV_1 and dV_2 :

$$\mathbf{S} = \frac{1}{2} (\mathbf{E}_s \times \mathbf{H}_s^*) = \mathbf{e}_r \frac{\omega n_0 k}{2\mu_0} (\mathbf{e}_r \times \mathbf{A}_f) (\mathbf{e}_r \times \mathbf{A}_f^*) \quad (5)$$

$$= \mathbf{e}_r \frac{\omega n_0 k}{2\mu_0} \frac{\mu_0^2}{16\pi^2 r^2} \iint_{V_0 V_0} [\mathbf{e}_r \times \mathbf{j}(\mathbf{r}_1)] [\mathbf{e}_r \times \mathbf{j}^*(\mathbf{r}_2)] e^{-in_0 k \mathbf{e}_r \cdot (\mathbf{r}_1 - \mathbf{r}_2)} dV_1 dV_2 \quad (6)$$

$$= \mathbf{e}_r \frac{\omega n_0 k \mu_0}{64 \pi^2 r^2} (1 + \cos \theta)^2 \int_{V_0} \int_{V_0} j(\mathbf{r}_1) j^*(\mathbf{r}_2) e^{-i n_0 k \mathbf{e}_r \cdot (\mathbf{r}_1 - \mathbf{r}_2)} dV_1 dV_2 \quad (7)$$

In Equation (5), we used the vector triple product where one term is equal to zero due to orthogonality. For Equation (6), we used that \mathbf{j} has the same direction as \mathbf{E}_0 (Equation (1)) which is unpolarized or circularly polarized, therefore $\mathbf{E}_0 = 1/\sqrt{2}(\mathbf{e}_\perp + \mathbf{e}_\parallel)E_0 \rightarrow \mathbf{j} = 1/\sqrt{2}(\mathbf{e}_\perp + \mathbf{e}_\parallel)j$. This leads to two cross products $\mathbf{e}_r \times \mathbf{e}_\perp = 1$ and $\mathbf{e}_r \times \mathbf{e}_\parallel = \sin(\pi/2 - \theta) = \cos \theta$, as shown in Figure 1.

Next, we introduce the cutoff function V which is $V(\mathbf{r}) = 1$ if \mathbf{r} is inside V_0 and zero elsewhere and acts as a 3D aperture. It represents the shape and the volume of the modification and removes the limits of integration.

Furthermore, we perform a change of variables and get the corresponding volume element with the aid of the Jacobian $\mathbf{r}_2 = \mathbf{r}_1 - \mathbf{r} \rightarrow dV_2 = dV$. Also, the shorthand for the propagation constant $n_0 k = \beta_s$ is introduced in the exponent, and we write the integral from Equation (7) as

$$\int_{-\infty}^{\infty} \int_{-\infty}^{\infty} e^{-i \beta_s \mathbf{e}_r \cdot \mathbf{r}} V(\mathbf{r}_1) j(\mathbf{r}_1) V(\mathbf{r}_1 - \mathbf{r}) j^*(\mathbf{r}_1 - \mathbf{r}) dV_1 dV \quad (8)$$

$$= \int_{-\infty}^{\infty} e^{-i \beta_s \mathbf{e}_r \cdot \mathbf{r}} [(Vj) \star (Vj)] dV = |\mathcal{F}^3 \{Vj\}|^2 \quad (9)$$

One group of functions just depends on \mathbf{r}_1 and the other, which is complex conjugate, on $\mathbf{r}_1 - \mathbf{r}$, therefore the integral in dV_1 is actually the autocorrelation function $\int P(\mathbf{r}_1) P^*(\mathbf{r}_1 - \mathbf{r}) dV_1 = P \star P$. The second integral in dV turns out to be the 3D Fourier transform \mathcal{F}^3 . At last, we make use of the Wiener–Khinchin theorem $\mathcal{F}^3 \{P \star P\} = \mathcal{F}^3 \{P\} \mathcal{F}^3 \{P\}^* = |\mathcal{F}^3 \{P\}|^2$ and find that the far-field scattering pattern is proportional to the power spectrum of the current density in the volume.

To our knowledge, this elegant result has been derived for the first time but it has one disadvantage in it requiring knowledge of the specific realization of the stochastic functions $j(\Delta n, E_0)$. To deal with this inconvenience we will compute the expected scattering behavior of one scattering center by taking the ensemble average $\langle \mathbf{S} \rangle$ after inserting the current density. At first, this will deviate from our elegant result, but in the end the structure of this solution will be recovered. The ensemble average

$$\langle \mathbf{S} \rangle = \mathbf{e}_r \sqrt{\frac{\epsilon_0}{\mu_0}} \frac{n_0^3 k^4}{16 \pi^2 r^2} (1 + \cos \theta)^2 \int_{-\infty}^{\infty} e^{-i \beta_s \mathbf{e}_r \cdot \mathbf{r}} \langle (V \Delta n E_0) \star (V \Delta n E_0) \rangle dV \quad (10)$$

is applied only to the autocorrelation function because it contains the stochastically varying functions Δn and E_0 . We see that the whole scattering power scales with k^4 (and thus λ^{-4}) similar to Rayleigh-scattering as already mentioned by Marcuse.^[4]

From this point on, the factor in front of the integral will no longer change, therefore we introduce the shorthand notation

$$Q(\theta) = \sqrt{\frac{\epsilon_0}{\mu_0}} \frac{n_0^3 k^4}{64 \pi^2 r^2} (1 + \cos \theta)^2 \quad (11)$$

We insert the eigenmode expansion Equation (2), where the summation index belonging to \mathbf{r}_1 is denoted with μ and the

other one belonging to $\mathbf{r}_2 = \mathbf{r}_1 - \mathbf{r}$ is denoted with ν . Similarly, we denote the dependency of other functions on \mathbf{r}_1 or \mathbf{r}_2 with the subscript 1 or 2:

$$\langle \mathbf{S} \rangle = \mathbf{e}_r Q(\theta) \sum_{\mu, \nu}^{\max} \int_{-\infty}^{\infty} e^{-i \beta_s \mathbf{e}_r \cdot \mathbf{r}} \int_{-\infty}^{\infty} V_1 V_2 \langle c_{\mu} c_{\nu}^* \Delta n_1 \Delta n_2 \rangle E_{\mu} E_{\nu}^* e^{i \beta_{\mu} z_1 - i \beta_{\nu} (z_1 - z)} dV_1 dV \quad (12)$$

Due to their interaction, the only stochastic functions are Δn and c . Now we follow the argument of Marcuse^[5] that the amplitudes and the refractive index perturbations are uncorrelated:

$$\langle c_{\mu}(z_1) \Delta n_1 c_{\nu}^*(z_2) \Delta n_2 \rangle = \langle c_{\mu}(z_1) c_{\nu}^*(z_2) \rangle \langle \Delta n_1 \Delta n_2 \rangle \quad (13)$$

Furthermore, we assume that the phases of the complex field amplitudes are sufficiently random, so their product is always zero for unequal indices $\langle c_{\mu}(z_1) c_{\nu}^*(z_2) \rangle \delta_{\mu\nu} = \langle c_{\mu,1} c_{\mu,2}^* \rangle \delta_{\mu\nu}$. This property removes the summation over ν , and we can express the ensemble average of the pointing vector as

$$\langle \mathbf{S} \rangle = \mathbf{e}_r Q(\theta) \sum_{\mu}^{\max} \int_{-\infty}^{\infty} e^{i(\beta_{\mu} z - \beta_s \mathbf{e}_r \cdot \mathbf{r})} \int_{-\infty}^{\infty} V_1 V_2 \langle c_{\mu,1} c_{\mu,2}^* \rangle \langle \Delta n_1 \Delta n_2 \rangle E_{\mu,1} E_{\mu,2}^* dV_1 dV \quad (14)$$

Now we rewrite the exponent as a scalar product of two vectors:

$$i(\beta_{\mu} z - \beta_s \mathbf{e}_r \cdot \mathbf{r}) = i(\beta_{\mu} \mathbf{e}_z - \beta_s \mathbf{e}_r) \cdot \mathbf{r} = -i \Delta \beta_{\mu} \cdot \mathbf{r} \quad (15)$$

With this conversion, we recover the 3D Fourier transform \mathcal{F}_{μ}^3 , which is now dependent on the summation index μ and transforms from \mathbf{r} space to $\Delta \beta_{\mu}$ space. This is the space of the scattering vector added to the incident light to produce the change in direction as shown in Figure 1.

$$\langle \mathbf{S}(\Delta \beta) \rangle = \mathbf{e}_r Q(\theta) \sum_{\mu}^{\max} \mathcal{F}_{\mu}^3 \left\{ \int_{-\infty}^{\infty} V_1 V_2 \langle c_{\mu,1} c_{\mu,2}^* \rangle \langle \Delta n_1 \Delta n_2 \rangle E_{\mu,1} E_{\mu,2}^* dV_1 \right\} \quad (16)$$

The next step is to recover the autocorrelation of the whole integral. We process the autocorrelation function $\langle \Delta n_1 \Delta n_2 \rangle$ by splitting it into the autocovariance $C_{nn} = \langle \Delta n_1 \Delta n_2 \rangle - \langle \Delta n_1 \rangle \langle \Delta n_2 \rangle$ and the product of the mean values $\langle \Delta n_1 \rangle \langle \Delta n_2 \rangle$. This separates the deterministic mean from the stochastic part which is now represented by the autocovariance. We apply the same procedure to the slowly varying amplitude c to obtain its autocovariance C_{cc} and its mean $\langle c_{\mu,1} \rangle \langle c_{\mu,2}^* \rangle$ and get:

$$\begin{aligned} \langle c_{\mu,1} c_{\mu,2}^* \rangle \langle \Delta n_1 \Delta n_2 \rangle &= [C_{nn} + \langle \Delta n_1 \rangle \langle \Delta n_2 \rangle] [C_{cc} + \langle c_{\mu,1} \rangle \langle c_{\mu,2}^* \rangle] \\ &= C_{nn} C_{cc} + C_{cc} \langle \Delta n_1 \rangle \langle \Delta n_2 \rangle + C_{nn} \langle c_{\mu,1} \rangle \langle c_{\mu,2}^* \rangle \\ &\quad + \langle \Delta n_1 \rangle \langle \Delta n_2 \rangle \langle c_{\mu,1} \rangle \langle c_{\mu,2}^* \rangle \end{aligned} \quad (17)$$

When we insert this result back into Equation (16), we obtain four terms. We now assume that both stochastic processes are homogeneous, so their autocovariance is only dependent on \mathbf{r} and can be taken out of the integral $\int dV_1$. Then what remains inside is in all cases the autocorrelation function. Furthermore, we can write the autocorrelation separate from the autocovariance by using the convolution theorem $\mathcal{F}_{\mu}^3 \{AB\} = \mathcal{F}_{\mu}^3 \{A\} * \mathcal{F}_{\mu}^3 \{B\}$

$$\begin{aligned} \langle S(\Delta\beta) \rangle = & \mathbf{e}_r Q(\theta) \sum_{\mu}^{\max} \left[\mathcal{F}_{\mu}^3 \{C_{mn}\} * \mathcal{F}_{\mu}^3 \{C_{cc}\} * \mathcal{F}_{\mu}^3 \{(VE_{\mu}) * (VE_{\mu})\} \right. \\ & + \mathcal{F}_{\mu}^3 \{C_{cc}\} * \mathcal{F}_{\mu}^3 \{(V\langle\Delta n\rangle E_{\mu}) * (V\langle\Delta n\rangle E_{\mu})\} \\ & + \mathcal{F}_{\mu}^3 \{C_{mn}\} * \mathcal{F}_{\mu}^3 \{(V\langle c_{\mu}\rangle E_{\mu}) * (V\langle c_{\mu}\rangle E_{\mu})\} \\ & \left. + \mathcal{F}_{\mu}^3 \{(V\langle c_{\mu}\rangle \Delta n) E_{\mu}) * (V\langle c_{\mu}\rangle \Delta n) E_{\mu})\} \right] \end{aligned} \quad (18)$$

As the last step to simplify the equation, we use the Wiener–Khinchin theorem to turn the autocovariance into the absolute square of its Fourier transform which we call the variance spectral density function of the refractive index fluctuations S_{nn} or the mode power amplitude S_{cc} . The same procedure is applied to the autocorrelations to get their respective spectral densities. We arrive at the final most general result of the scattering problem for the expected scattering pattern:

$$\begin{aligned} \langle S(\Delta\beta) \rangle = & \mathbf{e}_r Q(\theta) \sum_{\mu}^{\max} \left[S_{nn} * S_{cc} * \left| \mathcal{F}_{\mu}^3 \{VE_{\mu}\} \right|^2 \right. \\ & + S_{cc} * \left| \mathcal{F}_{\mu}^3 \{V\langle\Delta n\rangle E_{\mu}\} \right|^2 + S_{nn} * \left| \mathcal{F}_{\mu}^3 \{V\langle c_{\mu}\rangle E_{\mu}\} \right|^2 \\ & \left. + \left| \mathcal{F}_{\mu}^3 \{V\langle c_{\mu}\rangle \Delta n) E_{\mu}\} \right|^2 \right] \end{aligned} \quad (19)$$

Our solution to the scattering problem is the sum of four terms, which all contain a deterministic diffraction part in the form of several power spectral densities. The influence of the stochastic processes appears as the convolution with the respective variance spectral density of the noise process. If it is far from its maximum value, for example, the dominant fluctuation wavelength is way larger than the wavelength of the scattering light, its shape can be approximated as a normalized radial exponential: $S_{xx} \propto \exp\{-|\Delta\beta|/\tau\}$.^[16]

The result of the scattering problem includes the transformation from real into $\Delta\beta$ space which has its point of origin at the pole of the sphere in Figure 1. Geometrically, all permitted vectors $|\beta_i|$ and β_s have their tips confined to a spherical shell with the radius $|\beta_i| = |\beta_s|$ centered on the scattering center, also shown in Figure 1. This stems from the restriction to elastic scattering of a monochromatic wave, which must obey the phase matching condition $\beta_i \mathbf{e}_z + \Delta\beta = \beta_s \mathbf{e}_r$. This means that the $\Delta\beta$ vector always has a z-component in the range $[-2\beta_s, 0]$, so it is either negative or zero, positive z-values are not accessible.

2.1. Approximations to Improve the Usability

The previously derived model is useful to calculate a scattering pattern if all properties of the modification are known. For the experimentally observed scattering patterns the shape of the modification and the power spectral densities depend on a variety of experimental parameters that are partially stochastic. To be able to compare experiment and theory, we need to make some simplifying assumptions.

The first simplification is that the fiber core has only a slightly different refractive index compared to the cladding (which is fulfilled in the experiment, see Section 3), so we can apply the weakly guiding case, where all propagation constants merge into one $\beta_{\mu} \approx \beta = n_0 k$.^[4] It follows that the 3D Fourier transform in Equation (19) no longer depends on μ . Also, we assume that the electric field across the modification is approximately constant,

which effectively turns all the modes into plane waves with the transversal electric field E and the amplitude $\langle c \rangle$. The induced mean refractive index difference $\langle \Delta n \rangle$ is also assumed to be constant. This enables us to factor out these constants including the integrated volume $V^2 = (\int V dV)^2$ from the scattering problem. Additionally, we use the distributive property of the convolution to pull $|\mathcal{F}^3\{V\}|^2$ out of the brackets. This leaves a term with the δ -function as the identity operation of the convolution:

$$\begin{aligned} \frac{\langle S \rangle}{Q(|E| |\langle c \rangle| \langle \Delta n \rangle V)^2} = & \mathbf{e}_r \frac{|\mathcal{F}^3\{V\}|^2}{V^2} \\ & * \left[\frac{S_{nn}}{\langle \Delta n \rangle^2} * \frac{S_{cc}}{|\langle c \rangle|^2} + \frac{S_{cc}}{|\langle c \rangle|^2} + \frac{S_{nn}}{\langle \Delta n \rangle^2} + \delta \right] \end{aligned} \quad (20)$$

We recall from Equation (10) that the θ dependence is due to polarization and can be suppressed by observing the scattering through a polarizer to obtain $Q(\theta) = Q$. This formula shows that under these simplifying assumptions the total scattering power of a modification scales quadratically with V , c & Δn . This property can act as a rule of thumb to estimate the scattering power of a modification and how to enhance or diminish the extent of light scattering. Additionally, the plane wave is no longer required to be a guided wave, therefore this formula can also be used to calculate the scattering of external waves, which pass through the fiber cladding from the outside.

2.2. Random-Shaped V

The preceding calculations assumed that the volume V of the ensemble of the scattering centers is always the same. If we want to find the expected value by averaging measurements, we also must consider that the shape of the scattering volume is changing: the surface is fluctuating about a mean. This can be implemented by applying the ensemble average in Equation (12) also to $V_1 V_2$ and assume it is uncorrelated to the refractive index fluctuations and mode amplitudes in Equation (13). Then $\mathcal{F}^3\{|V\}|^2$ in Equation (20) has to be replaced by $\langle \mathcal{F}^3\{|V\}|^2 \rangle \approx \mathcal{F}^3\{|V\}|^2 * S_{VV}$. We make the approximation, that it is sufficient to convolute the volume with the power spectrum of the surface fluctuations to account for the random shape.

3. Experimental Section

The fiber, a commercially available step index optical fiber (Nufern 20/400 Precision Matched Passive LMA Double Clad Fiber: Core [NA = 0.065, $\varnothing = 20 \mu\text{m}$], Cladding [NA = 0.46, $\varnothing = 400 \mu\text{m}$]), was clamped to a motorized xy-table. The transparent plastic fiber coating was removed, and femtosecond laser pulses were focused into the fiber core with an NA = 0.25 microscope objective. The laser was a Ti:Sapphire regenerative laser amplifier system (Spectra Physics, Spitfire) emitting pulses at $\lambda = 800 \text{ nm}$ with a duration of FWHM = 200 fs. A pulse energy of 2.5 μJ and 1 kHz repetition rate was used. A mechanical shutter was set to 2 s opening time, so the number of pulses per scattering center was approximately 2000. After one refractive index modification was induced into the fiber

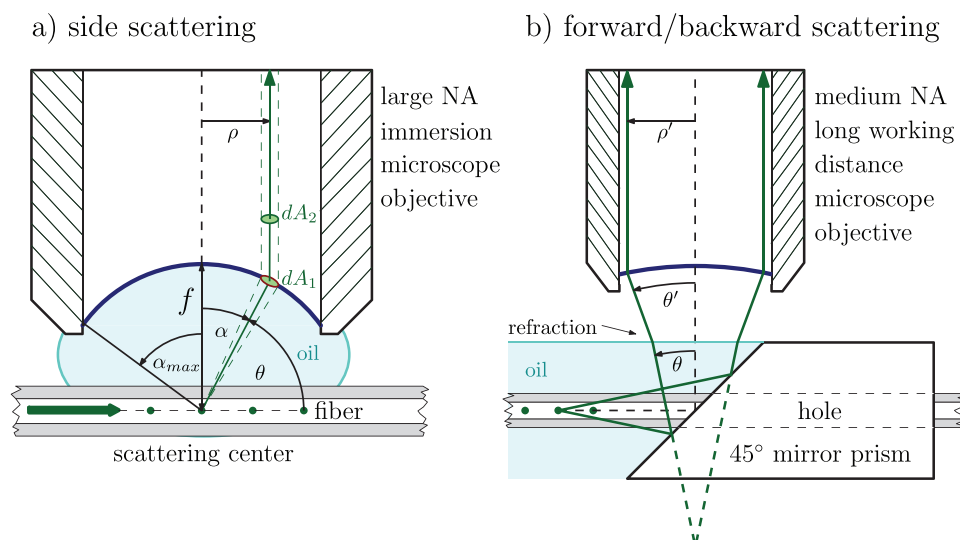


Figure 2. Fourier-microscopy for side, forward, and backward scattering. a) Rays spanning an angle α with the optical axis (dashed) are transformed into parallel rays with a distance ρ by refraction on the reference sphere (blue) according to the Abbe sine condition $\sin \alpha = \rho/f$. Glycerol ($n_0 = 1.46$) immersion eliminates refraction on the fiber surface. b) Rays with small scattering angles are reflected upward ($\alpha \rightarrow \theta$) by a 45° mirror and collected with a long working distance microscope objective. Backscattering is measured by reversing the mirror. Both set ups were calibrated with a diffuse transmittance standard (opal glass Qsil-ilmasil^[17]) to compensate for the objectives polarization dependent angular attenuation.^[18]

core, the fiber was moved and the procedure was repeated at a distance of $200 \mu\text{m}$ along the fiber. In this way, a chain of similar refractive index modifications was created in the fiber core. Sketches and images of the scattering center preparation can be found in ref. [11].

To measure the generated modifications and their scattering performance, the fiber was removed from the laser irradiation set up and coupled a green laser diode ($\lambda = 520 \text{ nm}$) with a maximum power of 100 mW into one fiber end. The initial linear polarization of the diode was converted to circular with the aid of a quarter wave plate. The modified fiber segment was then placed under a microscope (Jenapol Interphako), where the scattering of the light on the modifications as well as the refractive index distortions themselves was observed. For real space images, phase contrast objectives ($\text{NA} = 0.65$, $\text{Mag} = 40$) were used to enhance the visibility of the scattering centers.

The principle of the angular scattering measurement is shown in **Figure 2**. Here, the property that light in the front focal plane, by passing through the objective, is decomposed into its angular components whose intensity distribution is then projected onto the back focal plane, was made use of.^[7] This well-known behavior gives direct access to the far-field scattering pattern; it is often called the Fourier-transform capability of lenses, hence, the name Fourier microscopy. The back focal plane is imaged with the help of a Bertrand lens, which is placed in the beam path of the microscope^[19] (in polarization microscopy this method is also known as conoscopy). An $\text{NA} = 1.3$ oil immersion objective with a magnification of 100 was used for side scattering; for forward and backward scattering, a long-working-distance $\text{NA} = 0.6$ air objective with a magnification of 50 and a custom made mirror prism with a hole for the fiber was employed. Interference microscopy with the immersion objective was also used to approximate the induced refractive index change inside of the modification.

4. Results

The focused femtosecond laser irradiation produces a localized refractive index modification in the fiber core, which can be imaged with phase contrast microscopy, as shown in **Figure 3**. In all observed instances, the modifications have a very similar shape, but the interior consists of refractive index fluctuations which differ significantly from one modification to the next. This is readily visible in the side view of **Figure 3**. When comparing top and side-view, we find that the modifications are approximately ellipsoidal, with dimensions of $11.1 \mu\text{m}$ (length) by $15.2 \mu\text{m}$ (height) by $1.7 \mu\text{m}$ (width). In the inner regions, we determined an average refractive index change of $\langle \Delta n \rangle = 0.023 \pm 0.007$ relative to the fiber core by means of microscope shearing interferometry. When light of the green laser diode is coupled into the fiber, the refractive index distortion visibly scatters the light (**Figure 3** right). From this scattering image as well as the shearing microscopy we observe that the effective scattering volume might be smaller than the limits of the modification visible in phase contrast.

4.1. Scattering Pattern of a Single Modification

Light scattered by modifications in the core is transported away from the fiber with almost no refraction due to the index-matching oil. This light eventually forms the far-field scattering pattern of the chain of scattering centers. If one modification is placed in the focus of the high NA objective, its far-field scattering pattern can be observed individually. The two observation directions presented in Fourier space (**Figure 4**) correspond to the real space directions shown in **Figure 3**.

In side view the scattered light forms a pattern of smooth but otherwise random-shaped bright grains which are separated by

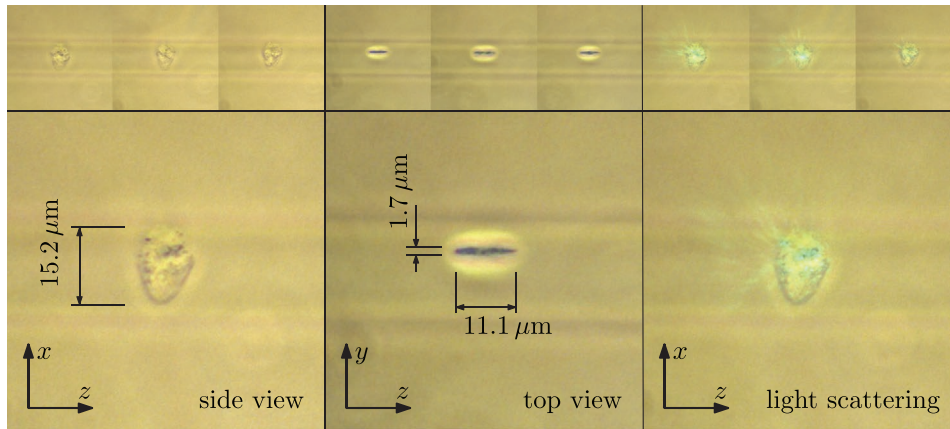


Figure 3. Phase contrast microscope images of the laser modifications in the fiber core. Top view is in the direction of laser irradiation and side view is orthogonal to it. Four images of similar scattering centers are provided (zoom in). The boundary of the fiber core shows up as two blurry horizontal lines in the background.

dark boundaries; a structure that is very similar to a laser speckle pattern. The grains are brighter on the right side (small θ) of the picture than on the left side (large θ), which means that the modification is predominately forward scattering.

In top view, we see a similar granular pattern to the broadside but with a wide dark band in the middle, crossing the picture horizontally. In the area of the dark band the grains appear less intense and vertically elongated. Also, the overall brightness in top view is lower than in side view: the imaging required roughly five times the exposure time.

Both pictures were taken with the analyzer polarization perpendicular to the direction of light propagation in the fiber while the light guided in the fiber is circularly polarized. If we set the analyzer polarization parallel to the fiber and look at the broadside of the scattering center, a vertical dark band appears in the center of the back focal plane image, crossing the image from the top to the bottom. This is a damping of the radiation which is strongest if the light is scattered perpendicular to the direction of propagation. The same phenomena of θ dependent damping is also observed for the small side and independent of fiber rotation around the z -axis (not shown).

4.2. Forward and Backward Scattering

Light scattered at very small or very large angles cannot be captured with the large NA immersion objective, because its opening angle is limited to $\alpha_{\max} = \pm 62.9^\circ$ ($27.1^\circ < \theta < 152.9^\circ$). To extend the observable angular range of the microscope, we used a mirror to reflect the forward and backward scattered light into the objective where we again image the back focal plane.

The images in **Figure 5** of forward (left) and backward (right) scattering show a central hole surrounded by concentric rings (very faint in backscattering). This pattern decreases in intensity and in distance in between the rings with increasing radius. Also, the brightness around the hole varies in magnitude: Its angular dependency is characterized by two bright lobes on opposing sides which are separated by a wider and dimmer scattering pattern.

The backward scattering shows almost now distinguishable pattern even though the exposure time in backscattering was 450 times longer than in forward scattering. Contrary to the side scattering in the previous subsection, the forward

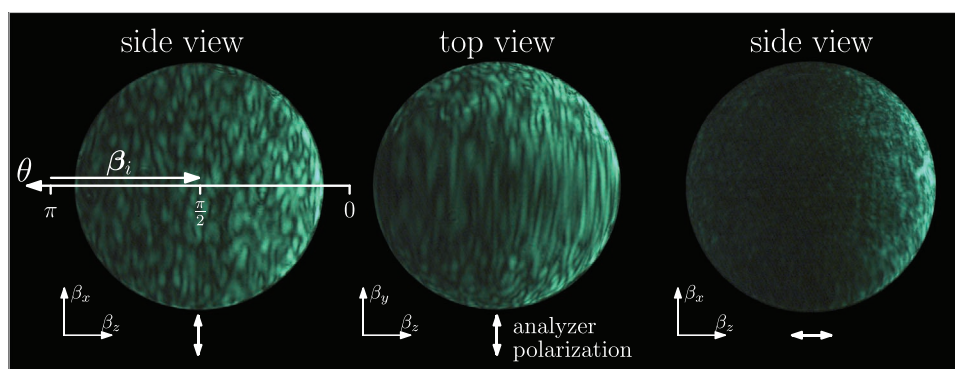


Figure 4. Back focal plane images of different perspectives and observation polarizations of the far-field scattering pattern from an excitation wavelength of 540 nm with circular polarization. Brighter colors mean more light exposure. The patterns were enhanced with histogram equalization, so they only allow for qualitative comparison. Views correspond to the real space images in Figure 3. Guided light crosses the pictures from the left to the right and is circularly polarized. Light on the right side of the circle is small angle forward scattering and on the left is large angle backward scattering. These images correspond to viewing the sphere from Figure 1 along the β_x - or β_y -axis.

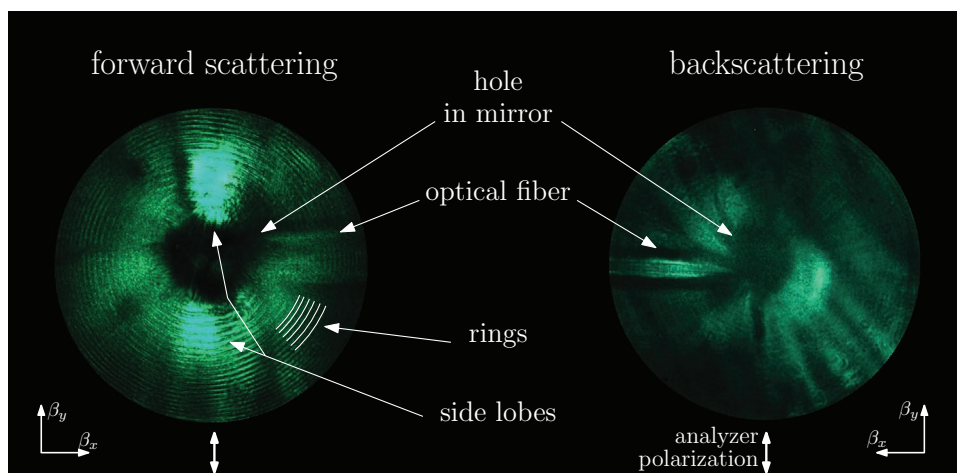


Figure 5. Forward and backward scattering pattern captured by reflecting the scattered radiation on a tilted mirror. In the middle of the picture is the hole where the fiber is threaded through the mirror (Figure 2). The optical fiber is bound by two dark horizontal lines and distorts the image beneath it. A pattern of concentric rings is centered on the hole, whose underlying intensity distribution shows an angular dependency: two bright lobes emerging from the hole pointing upward and downward. Rings in backscattering are very faint.

scattering does not show a strong polarization dependency in the intensity distribution on the picture.

The dark irregular shaped hole in the middle of the picture is where the fiber is threaded through the mirror. The fiber itself can be seen as two dark horizontal lines. In Section 5, it will turn out that the rings are probably a diffraction effect caused by the cylindrical shape of the fiber, they are not the main focus of this paper.

5. Discussion

The form of the scattering center is a product of overlapping femtosecond laser pulses in the focal spot in the core of the fiber. Before the focal spot is formed, the converging beam undergoes a refraction on the cylindrical fiber surface which introduces aberrations and turns the rotationally symmetric focal spot into a flat ellipsoid. Then, the overlapping of several laser pulses causes an evolutionary process inside the irradiated volume, which results in an average increase of the refractive index and the formation of stochastic fluctuations.^[20]

The change in refractive index is attributed to the generation of a hot electron plasma which quickly (<10 ps) transfers its energy to the glass matrix. Micro explosions^[21] for high pulse energies like in the present case produce random density fluctuations. It is well-known that fast heating and quenching leads to an increase in the glass' fictive temperature,^[22,23] which, in the case of fused silica, is associated with an increase in refractive index.^[13]

The measured mean value of $\langle \Delta n \rangle = 0.023$ is very high for a modification in fused silica created with a femtosecond laser. Typical values recorded on optical waveguides are in the range of up to 10^{-3} with a threshold value of 3×10^{-3} .^[24,25] When higher pulse energies are applied for inscription, the waveguides start to be too strongly scattering to be functional. Both the energy range and the scattering effect are consistent with the present light scattering modifications which were produced at 2.5 μJ .

5.1. Speckles

The far-field grain pattern which is observed in the back focal plane of the objective as shown in Figure 4 is the result of the interaction of the laser light with the refractive index distortion. The shape of the grains is very similar to a laser speckle pattern which can be observed when a rough surface interacts with coherent monochromatic light.^[26] Laser speckles are caused by the overlapping spherical wavelets with uncorrelated phase which are generated by multiple scattering regions on a rough surface.

In Section 2, we show that the pattern is a result of overlapping spherical wavelets generated by the interaction of the guided light with the refractive index fluctuations inside the modified volume. Also, due to the finite correlation length of the autocorrelation function, we obtain different contributing regions. We conclude that in the present case we generate volume speckles while common speckles are generated on a surface. The presence of speckles also signifies the spatial limitation of the (stochastic) interior of the modification: if the number of contributing regions would be large enough, the pattern becomes finer and smoothed-out; if there is a directional spatial limitation, the speckles get elongated as in the top view in Figure 4.

We also observe a strong dependency of the speckle pattern on polarization: one direction shows a strong θ dependency. This is a result of the $\cos \theta$ factor stemming from the polarization component \mathbf{e}_{\parallel} derived in Equation (7). Light, which is polarized parallel to the plane spanned by the incident and the scattered wave vector, cannot be scattered parallel to the polarization direction. This supports our idea that it is sufficient to image the \mathbf{e}_{\parallel} component of the scattering pattern via filtering to obtain an undisturbed picture. Furthermore, this is also in agreement with the observation that forward and backward scattering patterns have no polarization dependence because in this angular range the cosine is almost unity.

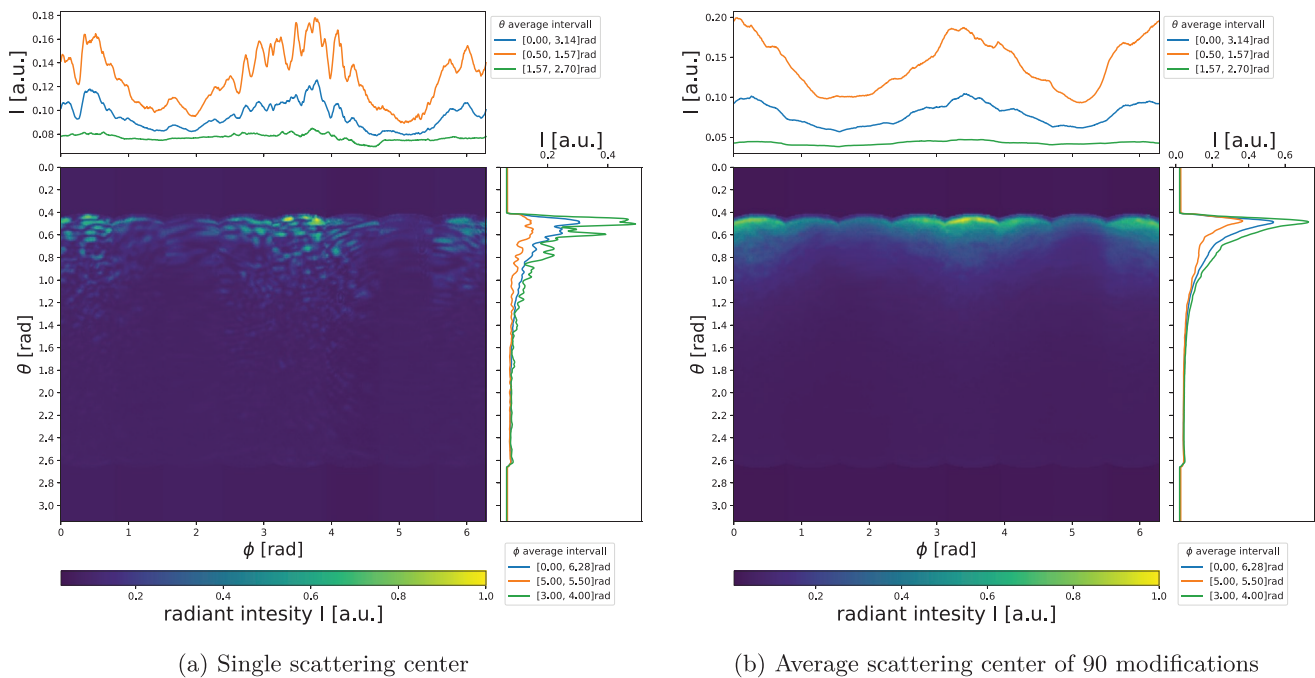


Figure 6. a) Maps of the far-field scattering pattern of a single modification assembled from eight back focal plane pictures which were imaged by rotating the fiber in steps of 45° . It shows the angular dependency of the far-field grain pattern. b) Average scattering map of 90 modifications. It shows the enveloping distribution which governs all scattering patterns. Both maps have constant spacing in polar θ and azimuthal ϕ angle.

5.2. Assembling an All-Around View and Averaging

The Fourier-plane images of Figure 4 show only a segment of the whole spherical far-field scattering pattern, which makes it difficult to compare the brightness of the angular distribution around the fiber. To obtain a more complete picture, we assembled a full 360° view in ϕ by stitching together 8 perspectives which were imaged in steps of $\Delta\phi = 45^\circ$. The result is shown in Figure 6. It represents a map of the far-field side scattering pattern, which is still limited to $0.47 < \theta < 2.67$ due to the maximum opening angle of the objective. Wrapping this map on a sphere comes closest to a true representation of the far-field scattering pattern where the modification is in the middle of the sphere as shown in Figure 1. The pattern itself consists of many small speckles. These are present on the whole map, but their brightness follows an enveloping pattern which depends on θ and ϕ . Their presence is harder to detect for large scattering angles θ without enhancing the contrast of the pictures as in Figure 4. We average the normalized maps of 90 similar modifications for an estimate of the enveloping intensity distribution. This leads to the smooth average distribution in Figure 6b.

Both maps show the same overall features in θ and ϕ : A strong increase in scattering power with decreasing polar angle θ , which means that the modifications are preferentially forward-scattering. Furthermore, the map shows a sinusoidal dependency of the brightness with the azimuthal angle ϕ . By comparing the real space and the Fourier images we find that the bright lobes coincide with the broad side of the scattering center and the dark bands with the small side of the scattering center. This is consistent with the forward scattering pattern which shows the same feature as the two side lobes.

For very large scattering angles ($\theta > \pi/2$), the far-field intensity approaches a low but constant value. This is the Rayleigh scattering background^[7] caused by the increase in glass' fictive temperature^[22,27,28] inside the modified volume. In the framework of our model, this can be treated as white noise background fluctuation which has a flat power spectrum.^[4] Rayleigh scattering has no angular dependency in the present polarization direction, so it is treated as an additive constant to the angular scattering pattern.

Comparison of the single and the average map shows four important properties: First, the grain pattern is the noisy power spectrum of one realization of the stochastic fluctuations inside the modification (Equation (9)). Second, the feature of two bright and two dark regions in ϕ as well as the increase in scattering for small θ is a general property that all scattering centers share. Third, the ϕ -dependency is a consequence of the ellipsoidal shape of scattering volume. Fourth, the decline of scattering power with θ is rotational symmetric in ϕ and therefore is caused by the radial functions S_{nm} and S_{cc} . The preferential forward scattering indicates that the power spectrum of the fluctuations has its maximum at way larger wavelengths than the scattered light. Therefore, it can be approximated by a radial exponential.

5.3. Computed Scattering Pattern

Having obtained the average scattering map, we now show that we can reproduce a qualitatively similar scattering pattern as laid out in Section 2. From Equation (20) we know that the average angular scattering distribution is caused by the superposition of four terms which all consist of a convolution with

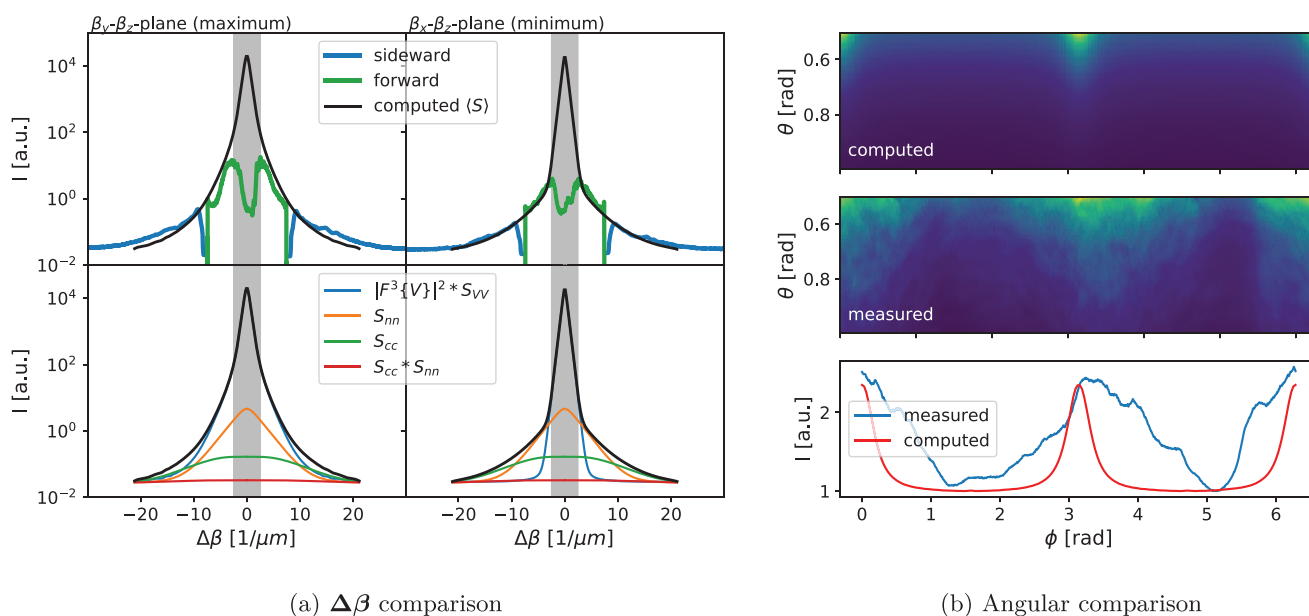


Figure 7. Comparison of the calculated scattering pattern with the experimental data. a) Top: Comparison of the $\Delta\beta$ dependency of the calculated scattering pattern with the measurements in forward and sideward scattering. The dip for small $\Delta\beta$ is due to the hole in the mirror (gray area). Bottom: Contributions of the convolution terms from Equation (20) to the computed cumulative scattering pattern (S). b) ϕ dependency of the calculated scattering pattern compared to the measured side scattering pattern. The patterns have been integrated with respect to θ to yield the graph at the bottom.

the absolute square of the 3D Fourier transforms of the modified volume $|\mathcal{F}^3\{V\}|^2$.

The first step of the computation is to define the computational volume: The edge length in real space ($l = 20 \mu\text{m}$) defines the smallest resolvable $\Delta\beta_{\text{min}} = 1/l$ vector due to the scaling property of the Fourier transform. The relation between the largest $\Delta\beta_{\text{max}} = \beta_i/2$ and the smallest defines the resolution $\Delta\beta_{\text{max}}/\Delta\beta_{\text{min}}$. Here the amount of computer memory available is the limiting factor for increasing the resolution because the data increases with the volume and therefore with resolution to the power of three (for this reason we choose only half of β_i to reduce computational effort). The modification is defined in the center of the computation grid as an ellipsoid ($1 = x^2/a^2 + y^2/b^2 + z^2/c^2$) with the semi-axis corresponding to the measurements from Figure 3: $a = 15.2 \mu\text{m}$, $b = 1.7 \mu\text{m}$, and $c = 11.1 \mu\text{m}$.

From this, we calculate the discrete Fourier transform and store it into an array. Additionally, we blur it with a normalized radial exponential S_{VV} ($\tau = 0.3 \text{ cm}^{-1}$) to account for the random surface. Then the three other terms are computed by calculating the convolution with two different normalized exponentials representing S_{nn} ($\tau = 2 \text{ cm}^{-1}$) and S_{cc} ($\tau = 3 \text{ cm}^{-1}$) (the latter just acts in the z-direction). The τ -values are chosen by hand to fit the measured curve and the results are weighted and added up. The final result is a 3D array in $\Delta\beta$ -space, where we find the observed scattering pattern by extracting only the values on the spherical shell from Figure 1 by interpolation.

The general trend for forward and side scattering is reproduced by adjusting the weight of S_{nn} to 5% and of S_{cc} to 3.5% of the deterministic diffraction pattern $\mathcal{F}^3\{|V\}|^2$. This is presented in Figure 7 where we compare the calculations to both measurements. Since the angular range for side and forward scattering doesn't overlap, both measured curves require different normalization. Two graphs on the top left show the scat-

tering power over $\Delta\beta$ in comparison to the calculation viewed as a slice through the maximum (β_y - β_y -plane) and minimum (β_x - β_y -plane). The contributions of the different convolutions are broken down in the corresponding images below: it shows that the expected scattering pattern for large $\Delta\beta$ is determined by S_{cc} ; for intermediate by S_{nn} and for small by $\mathcal{F}^3\{|V\}|^2 * S_{VV}$. The latter also causes the asymmetry between minimum and maximum. The $S_{nn} * S_{cc}$ term has almost no effect because it is too spread out.

Still, there are some noticeable deviations between computation and observation especially when we compare the whole map for sideward scattering in Figure 7 on the right. The modeled scattering lobes (maxima) are narrower than the observed ones even though they have almost the same amplitude. This is a consequence of the simple geometry of our calculated scattering center: the high aspect ratio of the ellipsoid leads to a very narrow diffraction pattern due to the reciprocal scaling property of the Fourier transform. This mismatch indicates that the real scattering center has a significantly more complex shape with a broader spectrum of large $\Delta\beta$ components. Nevertheless, even the chosen simple geometry reproduces the same general properties in ϕ and θ which were observed in the experiment.

All deviations from the ideal optical fiber scatter light, therefore the presented model also helps to understand the observations made by other researchers.^[8,9] Fonjallaz et al. and Janos et al. reported that light scattering of their fiber Bragg grating shows a similar azimuthal dependency with respect to the laser writing direction as in this experiment. We argue that this is also caused by the asymmetry of the refractive index modifications in the optical fiber; it is ultimately a consequence of the asymmetry of the focal volume: it is tighter focused in y than in z-direction due to the refraction of the femtosecond laser on the fiber surface. Consequently, the inverse scaling property of the

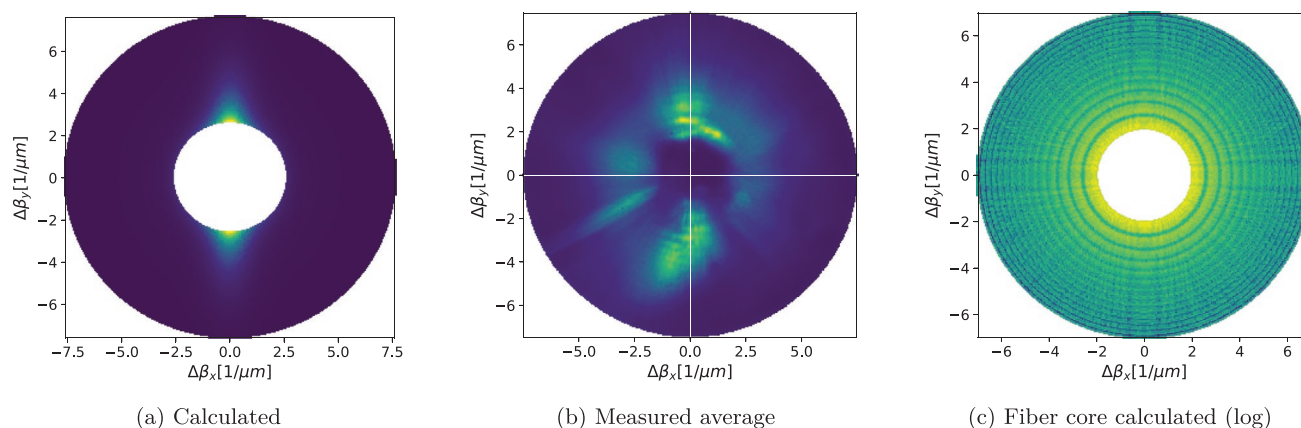


Figure 8. Images of the forward scattering pattern: a) Calculated scattering pattern for an ellipsoidal modification shows diffraction lobes but no ring structure. b) Measured average forward scattering pattern shows side lobes with visible rings. The white lines are the min/max cross sections where the forward scattering curves from Figure 7 were taken from. c) Calculated diffraction of a plane wave on the fiber core shows concentric rings (log scale).

Fourier transform turns the scattering pattern brighter in the direction of the smaller extent.

An important consequence of this finding is that the shape of the modification can be used to influence the ϕ -dependency of the scattering pattern: If one wants to have it constant in ϕ , the scattering center should be rotationally symmetric; if one wants to have a certain number of maxima in ϕ , the modification should reflect this requirement in its symmetry. On the other hand, homogeneous scattering in θ would require a flat power spectrum of S_{nm} in the range of the phase matching condition $[-2\Delta\beta, 0]$. As of writing this document, it is unknown how to selectively influence the spectra of the refractive index fluctuations with femtosecond laser irradiation. In a previous work,^[11] we found the maximum scattering loss for similar modifications to be around 900 nm, which means that a maximum of S_{nm} could be in that range. So, while the modification is predominantly forward scattering in the visible, in the near infrared it could already be homogeneous.

5.4. Forward Scattering Pattern

The concentric rings are the most prominent feature of the forward and backward scattering pattern. They were already observed by Rawson^[7] in his investigation of scattering loss in unmodified optical fibers. He gave the interpretation that they are the circular symmetric equivalent of laser speckles. If this explanation can also be applied in this case, then averaging several pictures of them should remove the rings and give us the enveloping function like in the previous subsections. The average intensity distribution from 100 different positions is shown in **Figure 8b**. It shows that even though the rings become less sharp, a visible ring pattern remains, which implies the presence of a deterministic diffraction pattern.

This is unlikely a product of the modifications themselves because when we compute the scattering pattern as in the previous section, we obtain the result shown in **Figure 8a**. Here, we see two lobes emerging from the center of the computed forward scattering pattern, which neatly correspond to the observed lobes in forward scattering. This is the pattern of the

modification. The two-lobe shape is again due to the reciprocal scaling effect of the Fourier transform, it causes the scattering to be dominant in the direction of the smallest extent of the modification in real space. In this way the elliptical cross section is imprinted on the forward scattering as it was the case for the side scattering. The difference between the computed and the observed scattering pattern is because the shape of the real scattering center is only approximately an ellipsoid as we already mentioned in Section 5.3. We additionally computed the diffraction pattern of two modifications with a distance of 200 μm , which shows the same two-lobe diffraction pattern (not shown), so we can rule out an interaction of several scattering centers.

Regarding an explanation for the circular ring pattern we argue that it originates either from the core-cladding or from the cladding-oil transition because it resembles an Airy disc. To demonstrate this in the framework of our present theoretical approach, we model the diffraction behavior by treating a section of the core itself as a refractive index distortion interacting with a plane wave. For modeling, we chose a cylindrical segment with a diameter of 20 μm and a length of 30 μm . The computational volume in real space was as long as the core segment in the z -direction but was extended to 80 μm in x and y . This zero padding was done in order to increase frequency resolution to help to resolve the ring pattern.

The result of the calculation is shown in **Figure 8c**. The diffraction pattern shows concentric rings whose distance and intensity decreases from the inside to the outside. From this similarity we conclude that the pattern could be caused by the fiber core itself. The light flux fueling this phenomenon is probably the main diffraction lobe of the modification which is shown in **Figure 7a** but cannot be observed due to experimental restrictions (the hole in the mirror). This would make this a very low angle scattering effect no longer covered by the volume current method. This almost unknown effect could have implications for the development of long period fiber gratings because it could influence the coupling from core to cladding modes.^[29]

There is certainly much ambiguity in setting the values of the equations. The problem at hand is that very little independently

measured data are available on the properties involved in the scattering process, especially the mean refractive index change and its variance. Nevertheless, future experiments could extract the power spectrum of the fluctuations from a fiber transmission measurement. Then the volume and the average refractive index change can be measured with microscopy techniques and the resulting scattering pattern could be calculated with less ambiguity and compared to the scattering measurements.

6. Conclusions

In conclusion, we derived an equation for the scattering pattern of a stochastic refractive index distortion of arbitrary shape in an optical fiber. This enables the calculation of the angular emission behavior as well as the interpretation of measurements for any kind of refractive index modification. The scattering power scales quadratically with the average induced refractive index change and the volume of the modification, which allows for precise quantitative control of the scattering process.

We experimentally determined the far-field scattering pattern of many similar refractive index modifications created with focused femtosecond laser irradiation: almost the full solid angle far-field scattering pattern was successfully imaged. This showed that while a single pattern is dominated by laser speckles, the average of several patterns follows an enveloping intensity distribution.

Several remarkable features of the scattering process could be assigned to different properties of the refractive index distortion by qualitatively comparing the calculated and the measured scattering patterns. We conclude that it is ultimately the shape of the scattering volume which determines the azimuthal dependency and that the power spectrum of the refractive index fluctuations determines the polar angle dependency. This property can now be used to engineer the angular distribution of the scattering pattern, which paves the way to a completely new class of tailored optical fiber emitters.

Acknowledgements

This work was funded within the Entrepreneurial Regions scheme of the German Federal Ministry of Science and Education (TOF-Tailored Optical Fibers). Further support was obtained from the Deutsche Forschungsgemeinschaft (DFG) (259607349/GRK2101). The authors thank Eva Schlindwein and Robert Röder for fruitful discussions, Thomas Kittel for assistance with optical microscopy, Lutz Preiser for metalwork, Gabi Möller for fabrication of the prism and Christian Zeidler for electrical work.

Conflict of Interest

The authors declare no conflict of interest.

Keywords

femtosecond lasers, light scattering, line sources, refractive index modification, side-emitting optical fibers

Received: April 14, 2020

Revised: May 29, 2020

Published online: June 26, 2020

- [1] A. Rendon, J. Okawa, R. Weersink, J. Beck, L. Lilge, in *Optical Methods for Tumor Treatment and Detection: Mechanisms and Techniques in Photodynamic Therapy XVI* (Ed: D. Kessel), International Society for Optics and Photonics, Proc. SPIE, Vol. 6427, Bellingham, WA **2007**, p. 64270M.
- [2] B. C. Wilson, M. S. Patterson, *Phys. Med. Biol.* **2008**, *53*, R61.
- [3] A.-A. Yassine, L. Lilge, V. Betz, *J. Biophotonics* **2018**, *12*, e201800153.
- [4] D. Marcuse, *Principles of Optical Fiber Measurements*, Elsevier, New York **1982**.
- [5] D. Marcuse, *Theory of Dielectric Optical Waveguides*, 2nd ed., Academic Press, New York **1991**.
- [6] Z. Pan, L. Wondraczek, *Sci. Rep.* **2018**, *8*, 9527.
- [7] E. G. Rawson, *Appl. Opt.* **1972**, *11*, 2477.
- [8] M. Janos, J. Canning, M. G. Sceats, *Opt. Lett.* **1996**, *21*, 1827.
- [9] P. Fonjallaz, H. G. Limberger, R. P. Salathe, *J. Lightwave Technol.* **1997**, *15*, 371.
- [10] L. Vesselov, W. Whittington, L. Lilge, *Appl. Opt.* **2005**, *44*, 2754.
- [11] A. Reupert, M. Heck, S. Nolte, L. Wondraczek, *Opt. Mater. Express* **2019**, *9*, 2497.
- [12] Y. Li, T. G. Brown, *J. Opt. Soc. Am. B* **2006**, *23*, 1544.
- [13] J. W. Chan, T. Huser, S. Risbud, D. M. Krol, *Opt. Lett.* **2001**, *26*, 1726.
- [14] I. White, *IEEE J. Microwaves, Opt. Acoust.* **1979**, *3*, 186.
- [15] M. Kuznetsov, H. Haus, *IEEE J. Quantum Electron.* **1983**, *19*, 1505.
- [16] J. Hudson, *Q. J. Mech. Appl. Math.* **1968**, *21*, 487.
- [17] T. Kreuzberger, *US Patent App.* 13/687,337, **2013**.
- [18] M. Leutenegger, R. Rao, R. A. Leitgeb, T. Lasser, *Opt. Express* **2006**, *14*, 11277.
- [19] J. A. Kurvits, M. Jiang, R. Zia, *J. Opt. Soc. Am. A* **2015**, *32*, 2082.
- [20] K. Itoh, W. Watanabe, S. Nolte, C. B. Schaffer, *MRS Bull.* **2006**, *31*, 620.
- [21] E. N. Glezer, E. Mazur, *Appl. Phys. Lett.* **1997**, *71*, 882.
- [22] M. Lancry, E. Réginié, B. Poumellec, *Prog. Mater. Sci.* **2012**, *57*, 63.
- [23] T. Seuthe, A. Mermillod-Blondin, M. Grehn, J. Bonse, L. Wondraczek, M. Eberstein, *Sci. Rep.* **2017**, *7*, 43815.
- [24] D. Homoele, S. Wielandy, A. L. Gaeta, N. F. Borrelli, C. Smith, *Opt. Lett.* **1999**, *24*, 1311.
- [25] S. Nolte, M. Will, J. Burghoff, A. Tuennermann, *Appl. Phys. A* **2003**, *77*, 109.
- [26] J. C. Dainty, *Laser Speckle and Related Phenomena*, Topics in Applied Physics, Vol. 9, Springer, New York **1975**.
- [27] M. Lancry, B. Poumellec, J. Canning, K. Cook, J.-C. Poulin, F. Brisset, *Laser Photonics Rev.* **2013**, *7*, 953.
- [28] B. Champagnon, L. Wondraczek, T. Deschamps, *J. Non-Cryst. Solids* **2009**, *355*, 712.
- [29] M. Heck, G. Schwartz, R. G. Krämer, D. Richter, T. A. Goebel, C. Matzdorf, A. Tünnermann, S. Nolte, *Opt. Express* **2019**, *27*, 4292.